Atmospheric-Turbulence Compensation Experiments Using Synthetic Beacons

Byron G. Zollars

Atmospheric turbulence limits the ability of ground-based telescopes to form images of astronomical or orbiting objects. Turbulence effects also decrease the on-axis intensity of laser beams propagated from ground to space. Conventional adaptive optics systems typically compensate for the deleterious effects of the atmosphere by sensing the wavefront of light originating at or near the object of interest, and correcting for it in real time. If the object is dim, however, conventional adaptive optics techniques fail. Recent experiments at the Lincoln Laboratory Maui Field Site have shown that Rayleigh backscatter from laser beams focused at altitudes up to 8 km can be used to generate beacons for an adaptive optics system; this process relaxes the requirements on object brightness. Synthetic-beacon adaptive optics technology can be applied to space surveillance, ballistic-missile defense, anti-satellite systems, and ground-based astronomy.

A FUNDAMENTAL PROBLEM in an adaptive optics system is measuring the distortion caused by atmospheric turbulence [1]. To accomplish this measurement, a source of light called a *beacon* must be located above the turbulent layers of the atmosphere and along the line of sight of the telescope. Sometimes light from the object being viewed can act as the beacon, such as with bright astronomical objects, sun-illuminated satellites, satellites that carry an on-board light source, or satellites with retroreflectors that can be illuminated from the ground by a laser. Frequently, however, the specific object of interest is not bright enough to serve as a beacon. In this case a bright star located in the same part of the sky as the object of interest can be used as a beacon. This *guide star* must lie within the isoplanatic angle of the object; that is, the star and the object of interest must be close enough in angle so that their rays experience essentially the same turbulence distortion through the atmosphere. At visible wavelengths the isoplanatic angle is only 10 to 20 μrad (2 to 4 arc sec). Thus the probability that a suitably bright guide star will be found within an isoplanatic angle of an arbitrary object is quite low.

How then can we use adaptive optics for atmospheric compensation when a suitable beacon is not available? The answer is to produce a synthetic beacon that can be created at will and placed as close as desired to the object of interest [2, 3]. The synthetic beacon is produced by projecting a laser beam into the atmosphere and using the backscatter from atoms or molecules as the source of beacon light for the adaptive optics system.

Our group at Lincoln Laboratory recently completed a series of atmospheric-compensation experiments with a synthetic-beacon adaptive optics system [4]. These experiments, called Short-Wavelength Adaptive Techniques (SWAT), were conducted at the Air Force Maui Optical Site (AMOS) atop Mount Haleakala on the Hawaiian island of Maui, where we used Rayleigh backscatter from a pulsed laser to measure distortion induced by atmospheric turbulence.

SWAT demonstrated what we believe to be the first use of a synthetic beacon to compensate a stellar image for atmospheric turbulence. We also performed the first experiments demonstrating atmospheric compensation of a stellar image by using multiple synthetic beacons.

One of the major objectives of the SWAT program was to develop and then demonstrate the technology necessary for compensating for the effects of atmospheric turbulence on laser beams originating from a ground transmitter and propagating to low-earth-orbit satellites. In fulfilling this objective, we demonstrated the first use of synthetic beacons to compensate a laser-beam uplink to a low-earth-orbit satellite. The laser-beam compensation was demonstrated by using a detector array on the Low-Power Atmospheric Compensation Experiment (LACE) satellite to measure the quality of the correction directly [5].

These atmospheric-compensation techniques were originally developed for use in the Strategic Defense Initiative ballistic-missile defense system, but are equally applicable to the imaging of astronomical objects with ground-based telescopes. An adaptive optics system like SWAT installed on a ground-based telescope has the potential to produce images in the visible part of the spectrum with angular resolution approaching the diffraction limit of the instrument. In addition, synthetic beacons greatly increase sky coverage by significantly easing the requirement for relatively bright guide stars close to the object of interest [6].

In this article, I describe what synthetic beacons are, how they are used to measure atmospheric distortion, and how they were implemented in the SWAT adaptive optics system. Because the results of the propagation experiments to the LACE satellite remain classified, this article emphasizes the results from the stellar-imaging experiments.

Synthetic Beacons

There are currently two approaches for the creation of a synthetic beacon. The first approach uses Rayleigh backscatter of laser light from the molecular constituents of the atmosphere [7]. The small cross section for this process, however, and the exponential decrease of atmospheric density with altitude combine to limit the practical altitude of synthetic Rayleigh beacons to 10 to 15 km (see the box entitled "Rayleigh Beacon Laser Requirements"). The Rayleigh approach is the one we used in the SWAT experiments.

The second approach uses resonant backscatter of laser light from the tenuous layer of atomic sodium located in the mesosphere at an altitude of 90 km [3, 7]. A beacon produced at this high altitude is advantageous because it reduces two major errors associated with a synthetic-beacon adaptive optics system. One error results from different paths through the atmosphere followed by rays from a beacon focused at a finite altitude and the collimated rays from an object farther out in space. The second error results from an inability to measure turbulence above the beacon altitude. These two errors are referred to together as *focal anisoplanatism.* Figure 1 illustrates how focal anisoplanatism arises.

Many measurements have been made of laser backscatter from the sodium layer [8, 9]. Nevertheless, in spite of the altitude advantage, a synthetic beacon based on sodium backscatter has not yet provided phase measurements for adaptive optics. The major challenge has been the need for a laser with relatively high pulse energy (a few Joules), a long pulse length (about 100 μsec), good beam quality, and precise spectral tailoring. Recent advances in solid state laser technology (most notably laser diode pumping) should make it easier to construct a laser with the necessary characteristics for use as a sodium-beacon source [10].

For the SWAT experiments, we chose Rayleigh beacons as the option with the lower risk, even though the energy requirements for the lasers necessary to produce Rayleigh and sodium beacons are of the same magnitude. Because Rayleigh scattering is nonresonant, spectral and temporal requirements did not drive the design of the beacon laser. In addition, when we planned the experiment the literature contained reports of lasers with energies in the 5-to-10-J range appropriate for use as Rayleigh beacon lasers [11], and commercial manufacturers were able to supply the components.

The SWAT Adaptive Optics System

The AMOS facility where the SWAT experiments took place is 3000 m above sea level and enjoys

RAYLEIGH BEACON-LASER REQUIREMENTS

FOR A FIXED telescope diameter, a specific number of wavefront-sensor subapertures, and a given Rayleigh backscatter signal level, the quality of atmospheric compensation in a synthetic-beacon adaptive optics system improves with a higher beacon altitude. To achieve a desired return signal, expressed as the number of detected photons per subaperture, we use the standard laser radar equation to compute the energy-per-pulse requirement for the Rayleigh beacon laser. This equation is

$$E = \frac{\gamma n^2 R^2 N}{\eta D^2 \tau_r \tau_t \tau_a^2(R) \rho_n(R) \sigma_\pi \Delta R},$$

where R is beacon altitude, N is the desired number of returned photons (per subaperture) at wavefront sensor, γ is the photon energy (equal to hc/λ), η is the detector quantum efficiency, D is the telescope diameter, n is the number of subapertures across the aperture diameter, τ_t is the optical transmission from beacon laser to atmosphere, τ_r is the optical transmission from telescope to wavefront-sensor entrance, $\tau_a(R)$ is the one-way atmospheric transmission, $\rho_n(R)$ is the atmospheric number density, σ_π is the Rayleigh backscatter cross section, and ΔR is the range gate distance.

The SWAT adaptive optics system requires approximately $N = 3000$ photons per subaperture [1] to make wavefront measurements with an accuracy of $\lambda/15$. By using typical values of the other parameters ($\eta = 0.7$, $n = 16$, $D = 60$ cm, $\tau_t = 0.3$, $\tau_r = 0.4$, $\Delta R = 0.1R$), we can compute the laser energy required as a function of beacon altitude. Figure A shows a plot of this energy. Note that the energy required from the beacon laser grows exponentially with increasing altitude. The difficulty of obtaining suitable lasers with tens of Joules of output energy limits the practical use of synthetic beacons formed by Rayleigh backscatter to altitudes below 20 km. A laser operating at $\lambda = 0.589$ μm, however, with an appropriate spectral envelope, can excite sodium atoms in the mesosphere at an altitude of 90 km. A synthetic beacon formed by resonant backscatter from the sodium layer uses laser energy more efficiently than a Rayleigh beacon above 10 km.

References

1. D.V. Murphy, "Atmospheric-Turbulence Compensation Experiments Using Cooperative Beacons," in this issue.

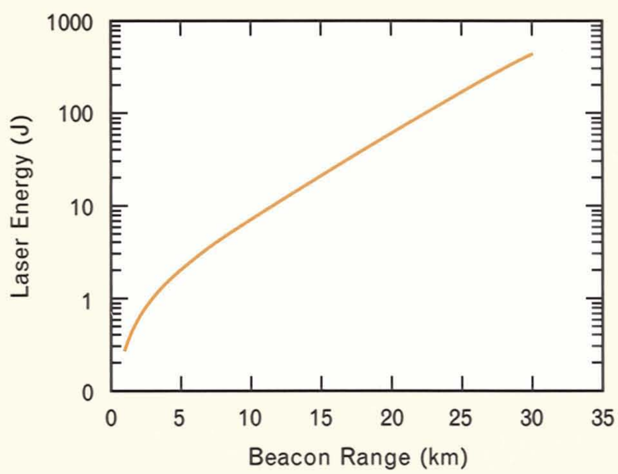

FIGURE A. Plot of beacon-laser energy needed to supply 3000 detected photons per subaperture to an adaptive optics system, as a function of beacon altitude. The graph assumes an adaptive optics system similar to SWAT, with a subaperture size of 3.75 cm, receiver transmission of 0.4, transmitter transmission of 0.3, detector quantum efficiency of 0.7, and range depth equal to 10% of the range.

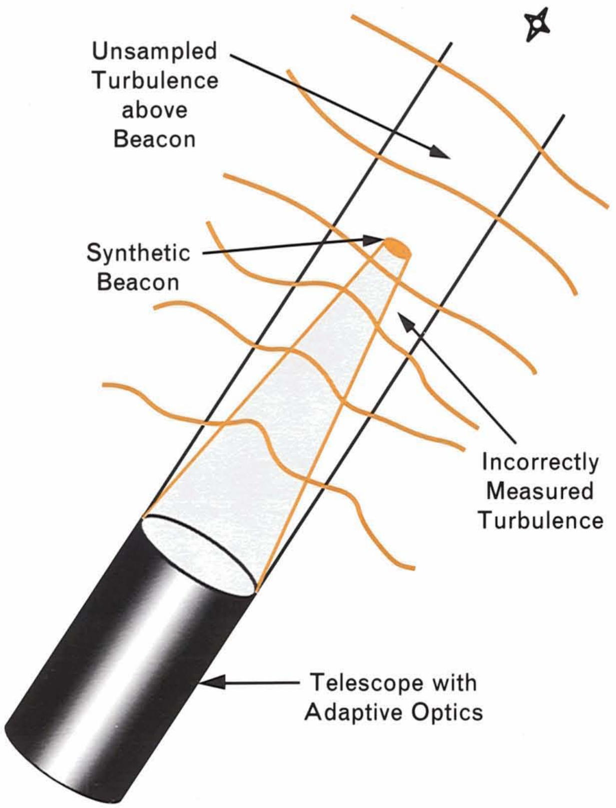

FIGURE 1. Focal-anisoplanatism error arises not only from the unsampled turbulence above the beacon altitude, but also from the portion of the turbulence below the beacon altitude that is sampled incorrectly because of the difference between the ray paths of the radiation from the beacon and the star.

frequent clear weather and good atmospheric seeing. Figure 2 shows a photograph of the facility. The main function of the facility is to perform precision optical tracking of satellites to determine their orbital parameters. To support this task, the site contractor maintains several optical telescopes and beam directors. For our experiments, we installed the adaptive optics system on one of the smaller telescopes, the Laser-Beam Director (LBD), which is shown in Figure 3. The LBD is a 60-cm-diameter stationary Cassegrain telescope with a 1-m-diameter pointing mirror mounted on an altazimuth bearing.

Figure 4 is a schematic representation of the system as configured for an astronomical imaging experiment using a synthetic beacon. The major adaptive optics components are a 241-actuator continuous-surface deformable mirror [12], a fast-steering mirror, a Hartmann wavefront sensor [13], and a digital wavefront reconstructor [14, 15]. These components are described in detail elsewhere [5]. With the exception of the deformable mirror, which was built by Itek, all of these components were built by Lincoln Laboratory. A photograph of the optical bench, with all of the adaptive optics components, appears in Figure 5.

The synthetic beacon is produced by a flashlamp-pumped pulsed dye laser ($\lambda = 0.512\ \mu m$), which is described later in this article. The linearly polarized output from the dye laser first passes through an adjustable lens that adds to the beam the amount of wavefront curvature necessary to cause it to focus at the correct altitude in the atmosphere. The laser beam is then injected into the optical train by transmission through a polarizing beam splitter. A quarter-wave retardation plate circularly polarizes the outgoing radiation. After propagating out from the telescope, the beam interacts with molecular nitrogen and oxygen in the atmosphere. The resulting Rayleigh backscatter, as it propagates downward from the backscatter altitude, picks up information about the turbulence-induced distortion and is collected by the telescope.

The backscattered beacon radiation reflects from the deformable mirror and the fast-steering mirror, then passes through the quarter-wave retarder. Because Rayleigh backscatter preserves polarization, the beacon light is still circularly polarized, and the quarter-wave plate transforms it to linearly polarized light with an orientation perpendicular to that of the outgoing laser radiation. With this orientation the returning radiation is reflected from the polarizing beam splitter. From there, the narrowband radiation passes through the dichroic mirror and a second adjustable lens. The lens removes the static focus on the beacon wavefront due to the wavefront's origination from a finite altitude. The focus-corrected beacon radiation then enters the wavefront sensor. The wavefront sensor measures phase gradients (i.e., local wavefront tilts) in both the x and y directions, at 218 locations over the aperture. The gradient measurements are made on a 16×16 rectangular grid, with the corners removed to conform to the round aperture. In the pupil plane of the telescope, the grid spacing corresponds to 3.75 cm.

The gradients measured by the wavefront sensor

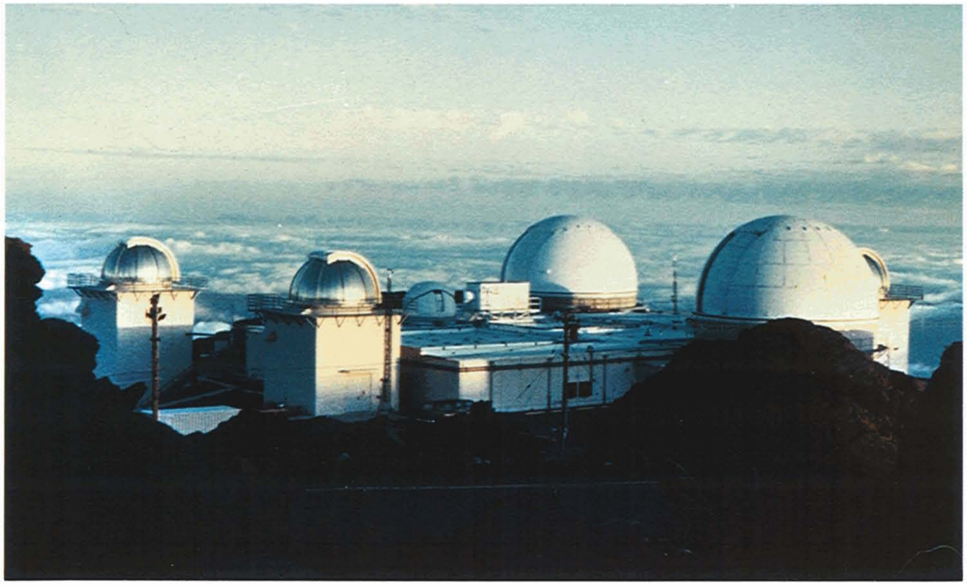

FIGURE 2. Photograph of the Air Force Maui Optical Site (AMOS) facility atop Mount Haleakala on the island of Maui. The facility is 10,000 ft above sea level. The numerous telescopes at the site are used for the facility's primary mission, which is the measurement of satellite orbital parameters.

are used by the phase reconstructor to calculate the distorted beacon wavefront. The phase at each position in the aperture can be expressed as a linear combination of all gradients. To yield a vector of phases, the reconstructor performs a digital multiplication of a matrix of precalculated coefficients by a vector of

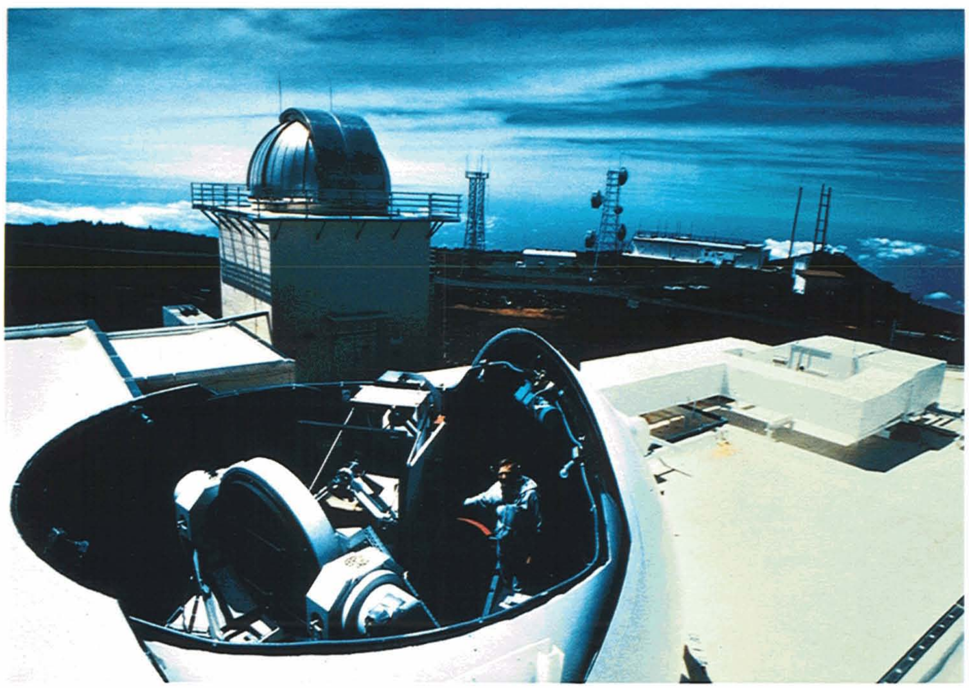

FIGURE 3. Photograph of the Laser-Beam Director, which is a 60-cm-diameter fixed Cassegrain telescope with a 1-m tracking flat. The tracking flat is mounted on a steerable altazimuth gimbal and is used to direct light into the telescope.

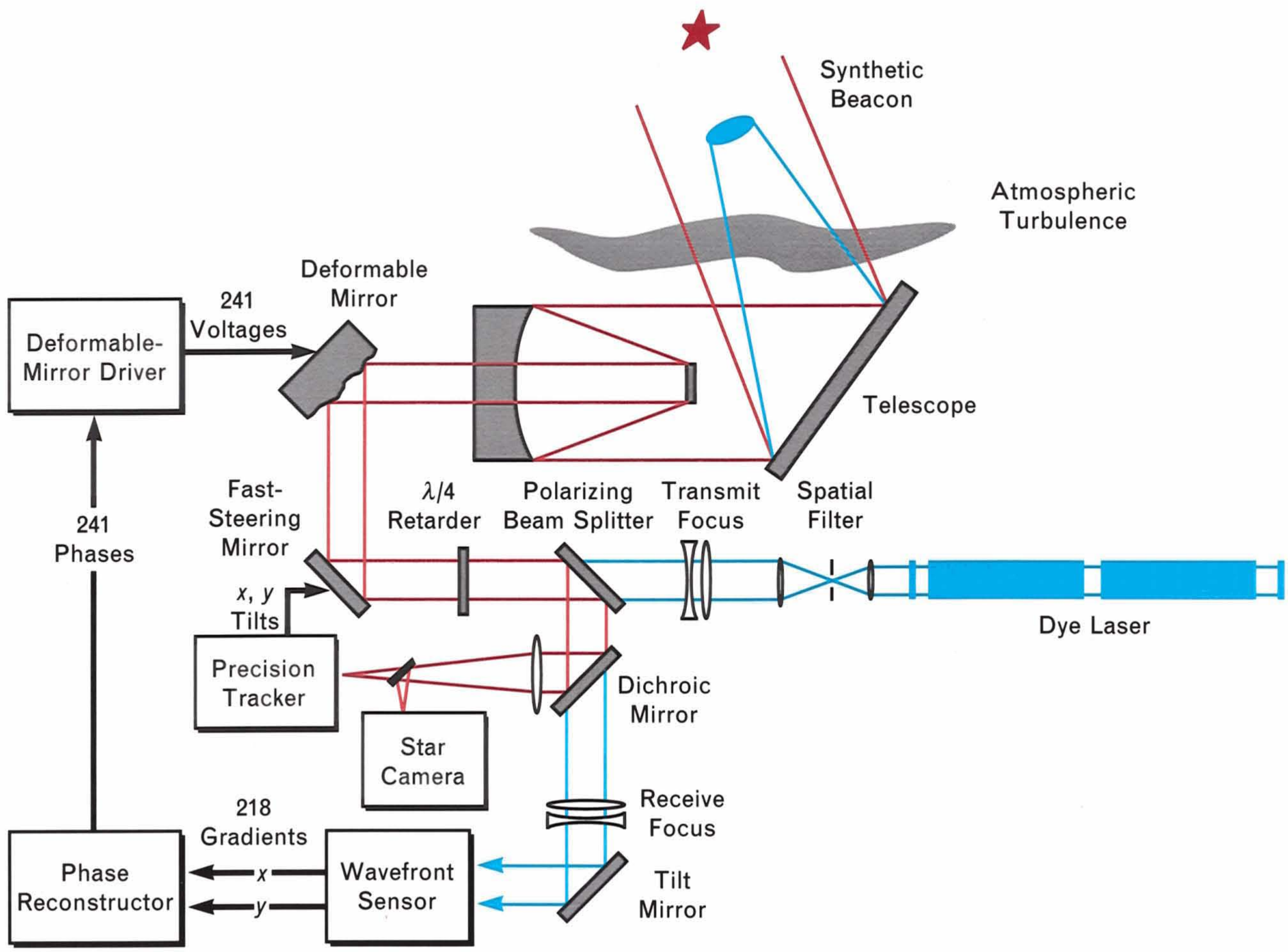

FIGURE 4. Schematic representation of the Short-Wavelength Adaptive Techniques (SWAT) adaptive optics system as configured for atmospheric-compensation experiments using a synthetic beacon.

the *x* and *y* gradients. Signals proportional to these phases are then sent to the deformable-mirror drivers, which in turn provide 241 voltages to drive the actuators on the deformable mirror. At this point, the deformable mirror takes on the proper figure needed to compensate the distortions in the atmosphere.

Light from the star, on entering the telescope, reflects from the deformable mirror and fast-steering mirror. It is then directed by the dichroic mirror to a focusing lens. A portion of the focused starlight is split off by a beam splitter and sent to a 64×64-pixel charge-coupled device (CCD) camera, whose field of view is 19 μrad. This camera records images of the star before and after we apply the phase correction to the deformable mirror. The measured on-axis intensity of the corrected image gives a measure of the quality of the phase compensation. Various optical coatings in the beam path limit the wavelengths reaching the star camera to two ranges, 0.40 to 0.50 μm and 0.55 to 0.60 μm.

Part of the starlight falls onto a precision tracker that uses a multiple-anode photomultiplier tube made by Hamamatsu. The tracker provides a direct measurement of the motion of the star image caused by the atmosphere and the telescope pointing error. This measurement is sent to a servo whose output drives the two-axis fast-steering mirror to keep the image of the star centered and stationary in the imaging camera. The closed-loop bandwidth of the tracking servo is selectable at 50, 225, or 600 Hz. When we compensate for tilt (i.e., image motion) separately with the fast-steering mirror, the phase dynamic range required of the wavefront sensor is reduced considerably, and the stroke of the deformable mirror is more effectively

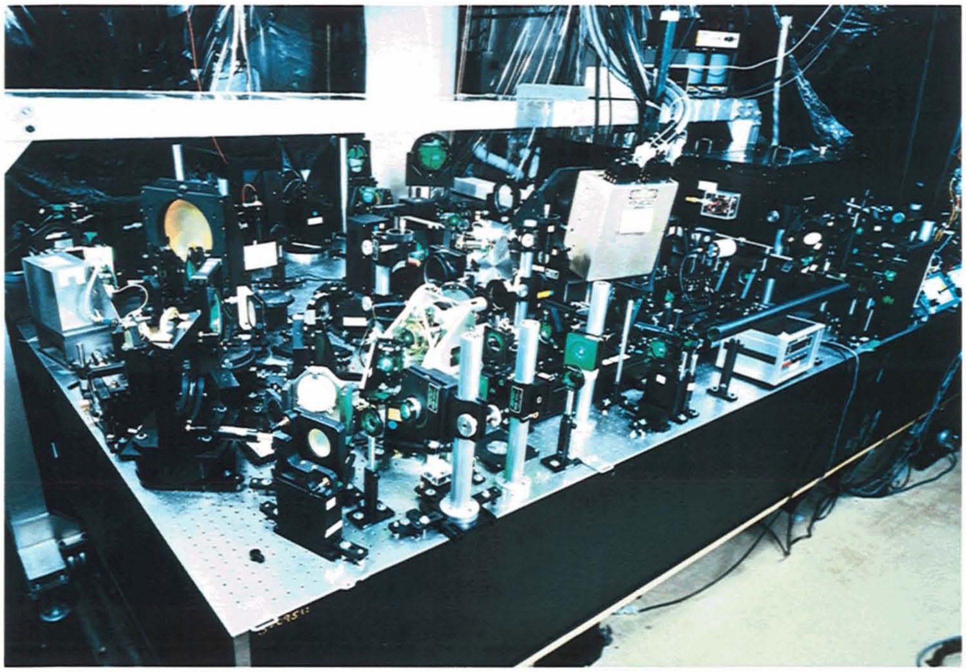

FIGURE 5. Photograph of the SWAT optical bench. The multitude of optical components mainly combine and magnify the beam. The deformable mirror is in the middle of the bench (with cables descending from the ceiling).

utilized for those aberrations of higher order than tilt.

The beacon laser is pulsed at a repetition rate (2 to 5 Hz) that is low compared to the rate at which the atmospheric distortion changes. Consequently, the adaptive optics system cannot use information from previous pulses in its determination of the phase correction. For an accurate correction in a single measurement cycle, the servo components (wavefront sensor, phase reconstructor, and deformable mirror) must all be absolutely calibrated (see the box entitled "Absolute Calibration of Adaptive Optics Components"). The *go-to* operation of the SWAT adaptive optics system, in which the deformable mirror must assume the correct phase-conjugate figure based on only one beacon wavefront measurement, differs from most systems that use a more conventional continuous-wave null-seeking servo. While calibration of the components makes the adaptive optics system more complex, it relaxes requirements on the repetition rate, and hence on the average power of the beacon laser.

The SWAT Dye-Laser System

The laser used in the SWAT synthetic-beacon experiments is a flashlamp-pumped pulsed dye laser. It is capable of a total energy of 6 J per pulse at repetition rates up to 5 Hz, with slightly lower energies at repetition rates up to 10 Hz. The beam quality of the dye laser, which is far from diffraction limited, is such that the total usable energy per pulse, defined for our purposes as the energy transmitted through a 20-λ/D spatial filter, is about 3 J per pulse. The lasing wavelength, which is selected by a dual-plate birefringent filter, is 0.512 μm, and the pulse duration is 2 μsec, measured at half maximum.

The dye laser is composed of two identical laser heads contained within the same optical resonator, as shown schematically in Figure 6. Each laser head is constructed from a tubular quartz dye cell, which is 60 cm in length and 1.2 cm in diameter. The dye solution that flows through this tube—50 μmoles/liter of Coumarin 504 dye in a solvent of 30% acetic acid amide in water—is excited by a pair of linear flashlamps in a close-coupled configuration. The flashlamps are mounted alongside the dye cell in a barium-sulfate-coated reflector housing. The four flashlamps together support an electrical discharge of

ABSOLUTE CALIBRATION OF ADAPTIVE OPTICS COMPONENTS

THE MAIN COMPONENTS of the SWAT adaptive optics system, which are used to compensate for the higher-order (above tilt) atmospheric aberrations, are the wavefront sensor, phase reconstructor, and deformable mirror. Because the atmospheric-compensation system operates in a pulsed mode, the components get only a single opportunity to make a wavefront measurement and apply the correct phase to the surface of the deformable mirror. Therefore, these components must be absolutely calibrated.

The wavefront sensor is calibrated by using a reference laser beam with a high-quality wavefront to which known amounts of tilt are added. The phase reconstructor is inherently calibrated by virtue of its digital computations. The deformable mirror, which consists of 241 discrete actuators (each with an analog driver), is the most difficult of the three components to calibrate; the stroke of each individual actuator must be linearized.

For calibrating the stroke of each actuator, the surface of the deformable mirror is measured with a Zygo interferometer interfaced to a host computer. Figure A is a diagram of the equipment setup for the calibration procedure. The surface figure measurements made by the interferometer are used for adjusting the voltage of each actuator to drive the surface of the deformable mirror toward flatness. This loop continues in an iterative fashion, until the mirror surface exceeds a flatness of $\lambda/50$ rms, or until some predetermined number of iterations have been completed. Figure B shows a representation of the surface profile after completion of the flattening procedure. The small-scale corrugation of the surface is due to the regular grid of actuators; the major contribution to the residual surface variation comes, however, from four actuators, just to the lower left of the center of the mirror. These actuators are slightly damaged and have a limited stroke, which prevents them from moving by the amount necessary to flatten the mirror completely.

After the flattening procedure, the voltage present on each actuator is recorded by the computer. The entire process is then repeated at several different values of the overall mirror piston. A poly-

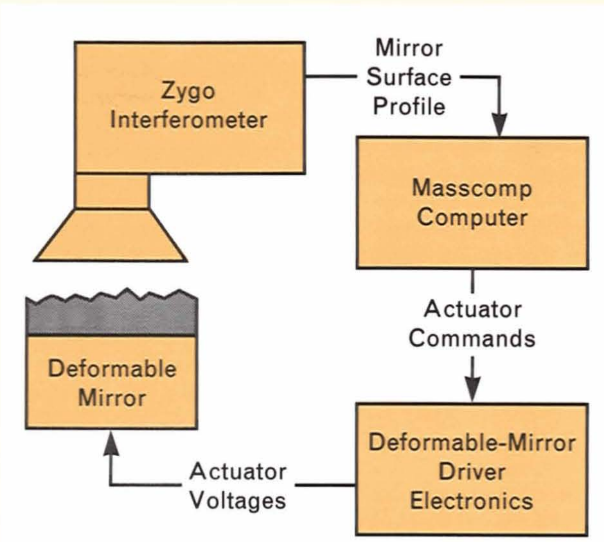

FIGURE A. Schematic diagram of the equipment setup used to calibrate the SWAT deformable mirror. Surface figure measurements made by the Zygo interferometer are used iteratively to flatten the mirror, and the voltage on each deformable-mirror actuator is then measured. Measurements over a range of mirror piston values yield the response function for each actuator.

nomial is fitted to the voltage-versus-stroke data for each of the 241 actuators, and these curve fits are then inverted and scaled to create the deformable-mirror calibration lookup table, which gives the digital command (proportional to the voltage) necessary to drive an actuator to a given absolute position within its stroke range. Figure C shows the stroke response data and polynomial fit for the central actuator in the SWAT deformable mirror. The calibration lookup table is loaded into the deformable-mirror drive electronics from the host computer prior to operation of the adaptive optics system.

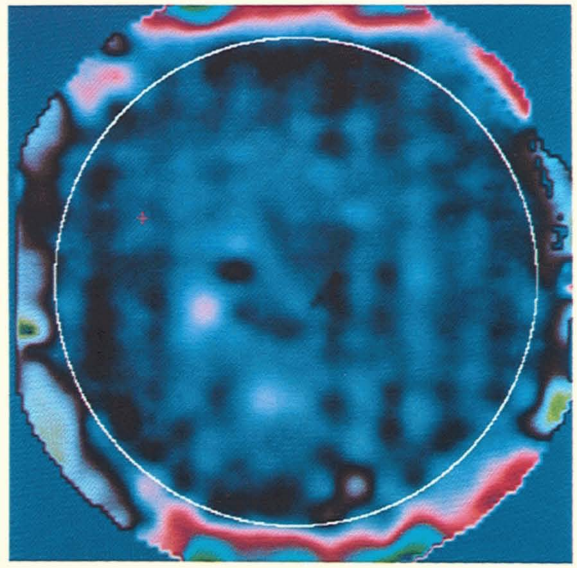

FIGURE B. Interferogram showing the profile of the deformable-mirror surface. The circle encloses the active area of the deformable mirror. In this photograph, the mirror has been flattened to a surface figure of approximately $\lambda/50$ rms.

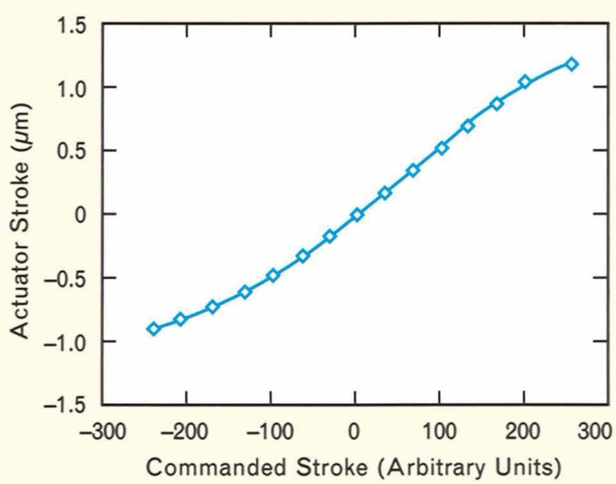

FIGURE C. Plot of the stroke response curve for the central actuator in the SWAT deformable mirror. This curve represents the motion of the actuator as a function of the applied voltage, which is directly proportional to the digital command given by the computer. The mirror calibration procedure results in a lookup table that, when loaded into the mirror-driver hardware, linearizes the stroke response curve for all actuators in the mirror.

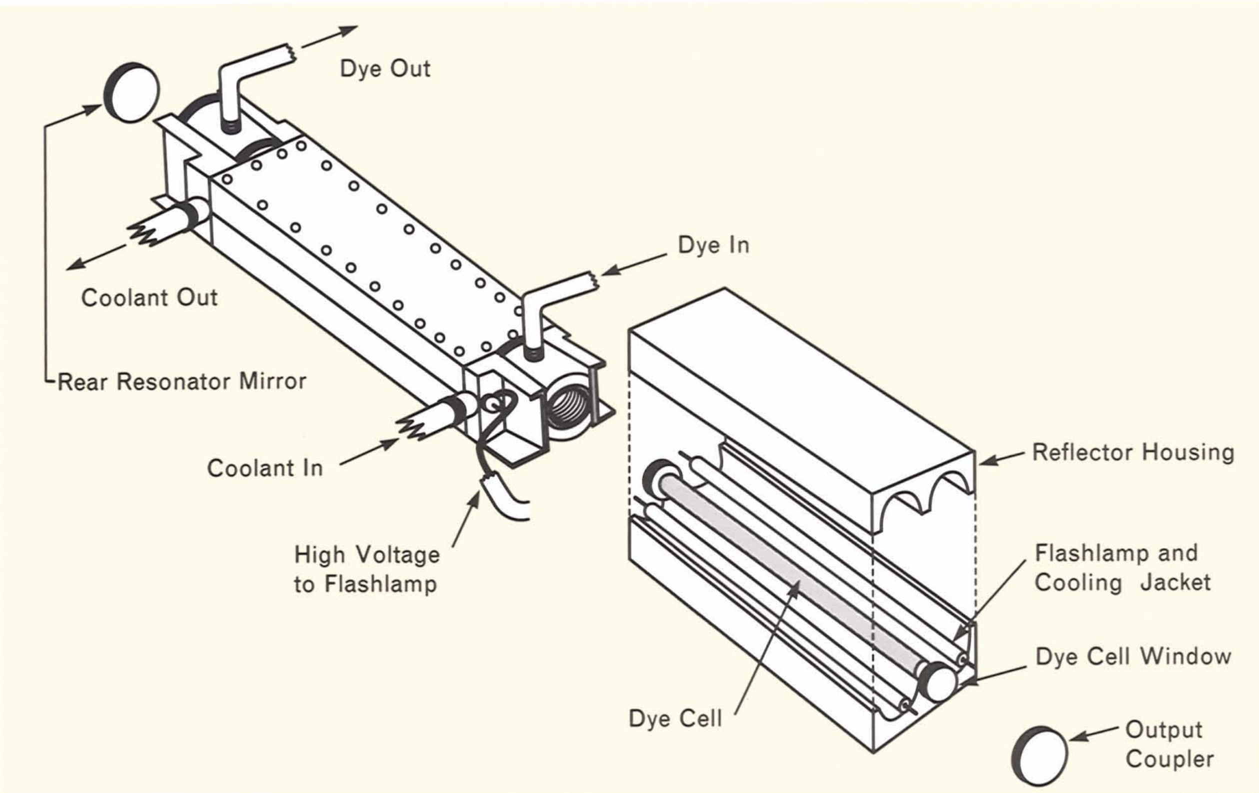

FIGURE 6. Schematic illustration of how a dye-laser head is constructed, and how two heads are combined to make up a single laser. Both laser heads are contained within an unstable optical resonator.

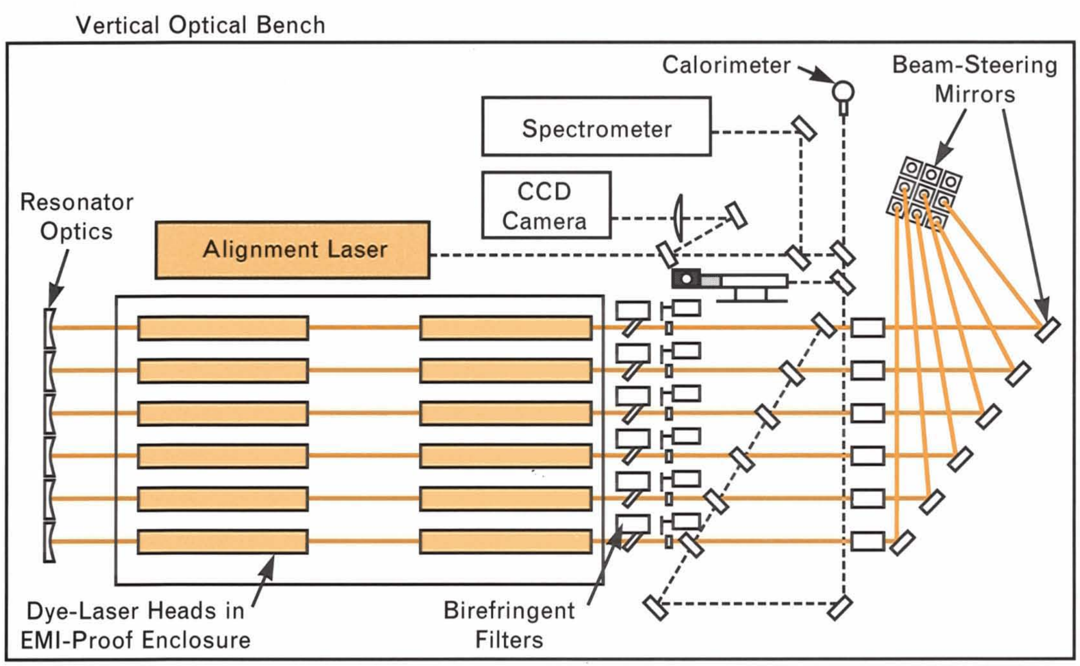

FIGURE 7. The vertical optical bench holds optics and diagnostics for six independent flashlamp-pumped dye lasers and their beam-steering optics. The laser diagnostics include measurements of pulse energy, spectral width, center wavelength, resonator alignment, and beam shape in the far field.

2000 J per pulse. A positive-branch confocal unstable resonator is used to allow efficient extraction of the energy contained within the relatively large lasing volume [16]. Water cooling is provided for the reflector housing by channels running the length of the head, and for the flashlamps by a coaxial Pyrex water jacket. The dye solution is pumped through the laser heads at a rate sufficient to ensure at least one replenishment of the dye cell volume between pulses, which minimizes residual thermal and photochemical effects. The flow rates of deionized cooling water and dye solution are 20 and 30 gallons per minute, respectively, for each laser head.

We built six of the dye lasers because, under some conditions, multiple synthetic beacons are needed to achieve good atmospheric correction. Our multiple-beacon experiments are described later in this paper. The lasers were installed together on a large vertical optical bench, along with their beam-steering optics. Figure 7 shows the layout of the lasers and the optics on the vertical bench. Holes in the vertical bench allow pipes to feed cooling water and dye solution to each laser head; other sets of holes carry the cables that supply high voltage to the flashlamps from the pulse-forming networks.

To prevent electromagnetic interference caused by the flashlamp discharge from affecting sensitive electronics throughout the facility, the lasers are housed in a shield room. All signals to and from this room, with the exception of the high-voltage power supply cables, are carried via optical fiber. The photograph in Figure 8 shows the shield room; visible in the back of the room is the vertical optical bench with the myriad pipes and cables for supplying dye solution and power to the individual laser heads. The blue boxes house the storage capacitors and pulse-forming networks for the flashlamps.

Combining this number of lasers presented many challenges. For example, the electrical power consumed by the flashlamps alone is 250 kW, which is

FIGURE 8. The dye-laser shield room protects sensitive equipment within the facility from electromagnetic emissions from the 2000-J flashlamp discharges. All electrical signals to and from the equipment in the shield room are carried by fiber optic cables, with the exception of the high-voltage power feed.

FIGURE 9. Photograph of the dye circulation pumps and main dye solvent reservoir. The vessel on the left is used for raw-solvent preparation and storage. This room is below ground level and all fluids drain by gravity into these vessels in the event of an emergency.

mostly dissipated as heat. Because exhausting this much heat into the air around the site would severely increase the local turbulence, all waste heat is dumped to an underground heat sink, a tank containing 10,000 gallons of chilled water. The water is cooled down during the day, and gradually warmed during nighttime experiments as heat is added.

The system dye flow capability is 360 gallons per minute, and the cooling-water flow capability is 240 gallons per minute. We used organic laser dye in kilogram quantities and designed special process equipment to facilitate its handling. Each batch of dye solution is approximately 1200 gallons, which is too much liquid to dispose of and replace on any regular basis. Instead, vessels holding activated charcoal cartridges stripped used dye and photodecomposition products from the solvent, allowing it to be recycled. Figures 9 and 10 show some of the equipment used for pumping, filtering, and cleaning the dye solution.

Figure 11 shows the major subsystems of the overall dye-laser system. We assembled the system from custom-built equipment supplied by different vendors. The laser heads are a heavily modified version of a commercial Candela Laser Corporation LFDL-20 flashlamp-pumped dye laser. Candela also supplied the basic circuitry for the pulse-forming networks that delivered energy to the flashlamps, although Maxwell Laboratories supplied important components such as the capacitors and spark-gap switches. ALE Systems supplied the high-voltage capacitor-charging power supplies and the DC simmer-discharge power supplies. Stone and Webster Engineering Corporation supplied the entire fluid-handling system, consisting of pressure vessels, piping, valves, pumps, and heat exchangers. A process/safety controller, designed and built at Lincoln Laboratory, tied the individual pieces of the system together, simplified the operation of the lasers significantly, and allowed for automated shutdown of all equipment in the event of an emergency. Interested readers can find more specific information about the laser system elsewhere [17].

As with anything that advances the state of the art, the SWAT dye-laser system was not without problems. For example, we had difficulty procuring optical coatings that could withstand the 10 J/cm^2 intracavity fluence. We also had problems with arcing in the high-voltage sections of the flashlamp energy-storage modules (40 kV at 10,000 ft above sea level!). These problems were solved, but we could never significantly improve the beam quality of the lasers. The poor beam quality reduced the usable laser energy and restricted the synthetic beacons to lower altitudes than we would have preferred.

Over the past few years, great advances have been made in solid state laser technology. A synthetic-beacon system based on Rayleigh scattering could now use frequency-doubled Nd:YAG lasers in place of dye lasers, with better performance, lower cost, and higher reliability.

Experimental Procedure

Prior to an atmospheric-compensation experiment, a star is selected and acquired with the telescope. Starlight passes through the telescope, is reflected off the (flattened) deformable mirror and the fast-steering mirror, and is directed into the Hamamatsu precision tracker. The angle of the fast-steering mirror is then adjusted continuously to keep the image centered in the tracker. To keep the fast-steering mirror from exceeding its range of travel, its average position is measured and used for dynamically biasing the pointing servo of the main telescope. Thus pointing errors with frequencies lower than 2 Hz are removed by the main telescope and errors with frequencies from 2 to 600 Hz are removed by the fast-steering mirror.

Once the precision tracker servo is engaged, and the star image is centered in the star camera, the compensation sequence is started. Figure 12 illustrates the sequence of events. First, the deformable

FIGURE 10. Photograph of the activated charcoal and filter vessels for stripping dye and decomposition products from the used solvent. Cleaning the dye solvent allows it to be used for subsequent experiments.

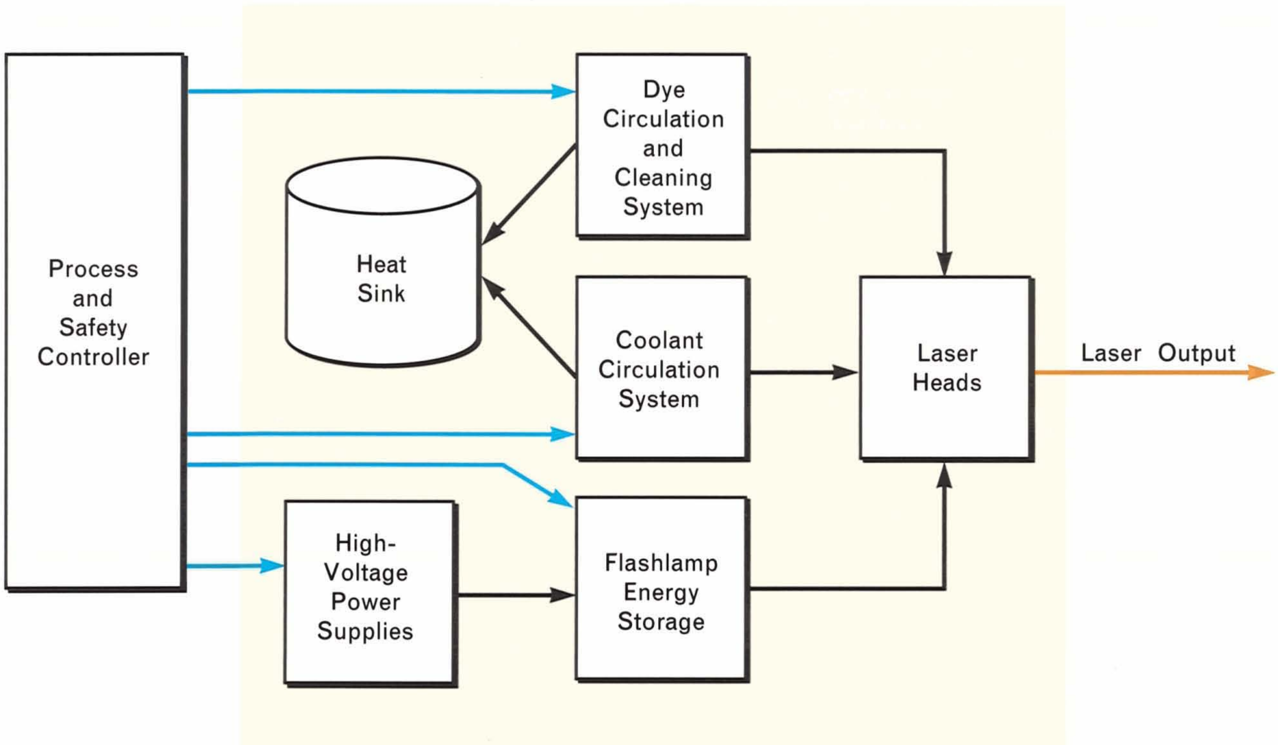

FIGURE 11. Block diagram of major dye-laser subsystems. A single computer controls all of the pumps, valves, and power supplies to ensure safe operation and quick shutdown of the entire system in the event of an accident.

mirror is commanded to be flat. About 150 μsec later, the deformable mirror has settled, and the star camera begins to integrate an uncompensated image of the star. This integration time is typically 1 msec but can be varied depending upon the brightness of the star. After the star camera data have been read out, the dye laser is fired. Because the telescope is focused at infinity to view the star, and the beacon must be focused at a finite distance from the telescope, an adjustable lens is used to add focus to the transmitted dye-laser beam. The altitude of the beacon focus varies between 6 and 8 km.

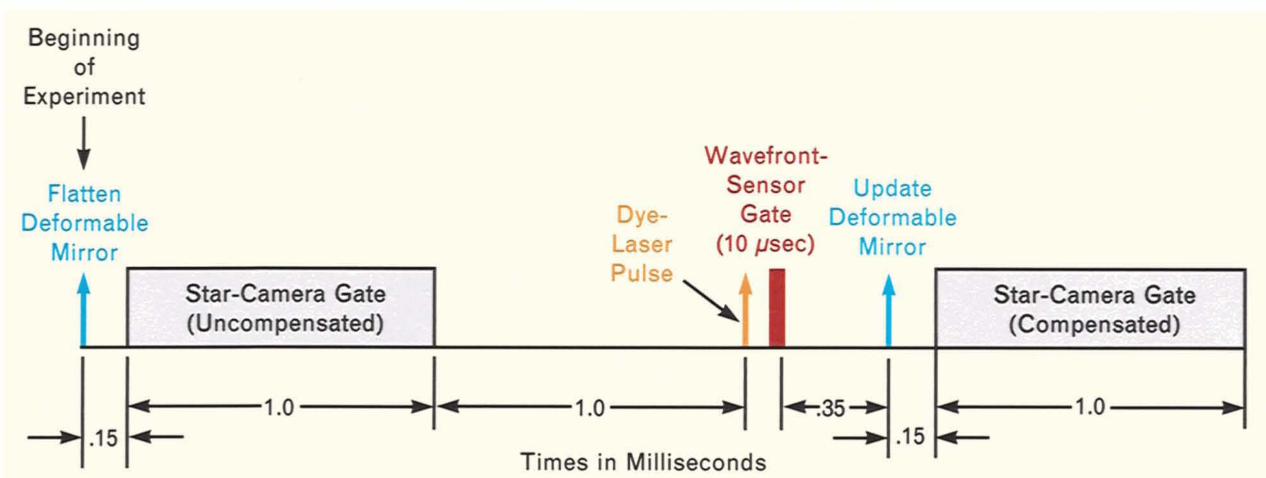

FIGURE 12. Event timeline for atmospheric-compensation experiments using a single synthetic beacon. This timeline is repeated at a repetition rate of 5 Hz during data collection.

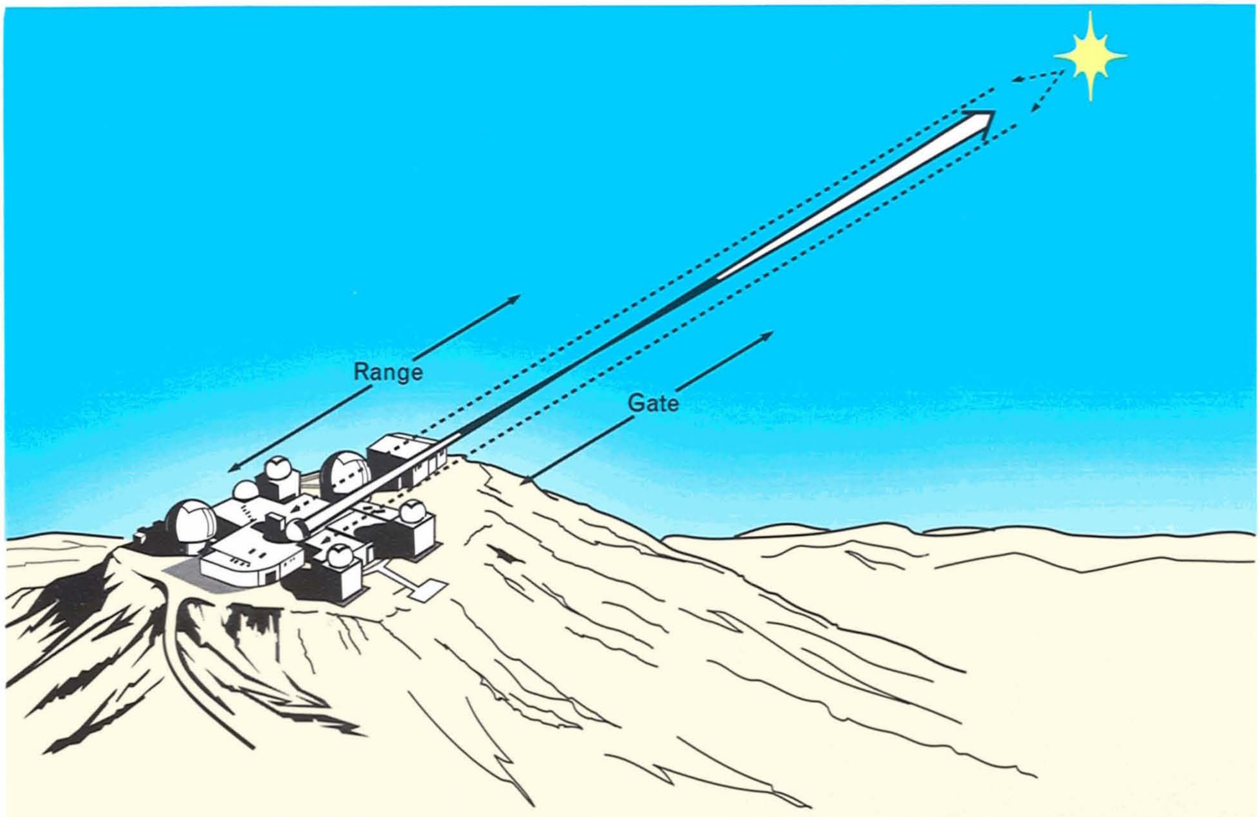

FIGURE 13. For most of the single-beacon experiments, the beacon was focused at a range of 6 km, with a range gate spanning 750 m below and above the region of focus.

After a time delay corresponding to the round-trip travel of light to the beacon altitude, the wavefront sensor is shuttered open with a Pockels cell, and the backscattered beacon radiation is collected to make the atmospheric distortion measurement. An adjustable lens in front of the wavefront sensor removes the focus on the received beacon radiation. The wavefront sensor typically integrates the backscattered synthetic-beacon radiation for 10 μsec, with the timing chosen such that the gate interval is centered on the beacon altitude range-delay time, as depicted in Figure 13. The resulting 218 x and 218 y measured wavefront gradients are then sent to the phase reconstructor as a digital data stream.

The phase value calculated for each of the 241 deformable-mirror actuators is sent directly to the deformable-mirror drive electronics. A 350-μsec delay is necessary to reconstruct the phase and apply it to the surface of the mirror.

After another 150-μsec delay to allow the deformable mirror to settle to the commanded figure, the star camera again integrates an image of the star, but now the image has been compensated for the atmospheric distortion. The above process, in which each cycle is an independent compensation experiment, is repeated at 2 to 5 Hz during a given run. Data are recorded as a pulse-code-modulated data stream on analog tape for long runs, or directly to computer disk for shorter runs.

Measurements of several important atmospheric parameters are made during experiments. Routine meteorological data such as wind speed and direction, temperature, and dewpoint are collected continuously by the AMOS contractor. We are also supplied periodically with measurements of the atmospheric coherence length r_0 [18] from one of the larger telescopes at the site. The r_0 parameter is a measure of the strength of the atmospheric turbulence; it represents the distance in the telescope aperture at which two measurements of phase become essentially uncorrelated. Smaller values indicate stronger turbulence. For a given turbulence distribution, r_0 varies as the

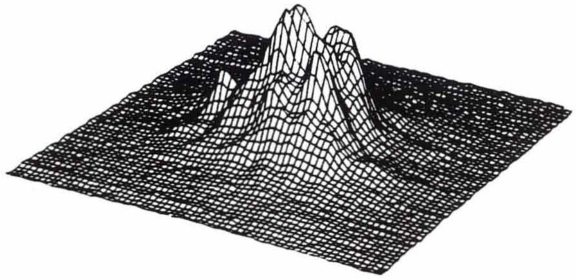

(a)

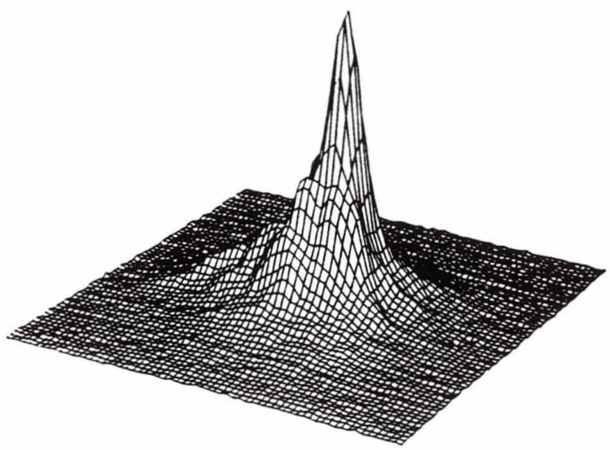

(b)

FIGURE 14. Images of the star Vega (α-Lyra), (a) uncompensated and (b) compensated for atmospheric distortion in experiments using a synthetic beacon. The data were taken on 25 August 1988, and are the first atmospheric-compensation results using a synthetic beacon. The field of view spans an angle of 19 μrad (4 arc sec).

6/5-power of the wavelength. For visible wavelengths, typical r_0 values at AMOS are from 5 to 12 cm.

The isoplanatic angle θ_0 represents the angle beyond which measurements of phase become uncorrelated. This angle, which also varies as the 6/5-power of the wavelength, is sensitive to turbulence at high altitudes. Typical values of θ_0 are between 5 and 20 μrad in the visible. We use a stellar scintillometer [19], supplied by the Naval Postgraduate School, for routine measurements of the atmospheric isoplanatic angle θ_0.

Experimental Results

Although the SWAT equipment was not designed with astronomy in mind, star-imaging experiments with one or more synthetic beacons were frequently conducted to assess the performance of the adaptive optics system. This section presents the results of some of these experiments. Although limited to bright objects because of the relatively small telescope aperture and narrowband optical coatings, our experiments demonstrated angular resolutions that could significantly benefit the astronomy community.

Compensation of Stellar Images

On 25 August 1988, we recorded the first stellar image ever compensated for atmospheric turbulence with a synthetic beacon. The object was Vega (α-Lyra), a bright star of visual magnitude 0.04. Figure 14 shows that the degree of compensation was relatively poor, corresponding to an increase of only a factor of two in peak brightness. Subsequent to the first experiments, improved equipment and accumulated experience allowed substantial improvements in the quality of the compensated images.

Figure 15 shows the compensated and uncompensated images of the star Procyon (α-Canis Minor), with a visual magnitude of 0.36, taken under measured turbulence conditions of r_0 equal to 9 cm and θ_0 equal to 19 μrad. The zenith angle of the star during these experiments was 20°. The wavefront-sensor gate duration corresponded to 1.5 km, and was centered on the beacon altitude of 6 km.

A common measure of the quality of an image is the Strehl ratio, which is defined as the ratio of the peak intensity to the diffraction-limited peak intensity. The Strehl ratio for the compensated image in Figure 15 is approximately 0.4, which is close to the best compensation expected for the adaptive optics system, in view of known error sources (see the box entitled "Sources of Error in Synthetic-Beacon Adaptive Optics"). As Figure 16 shows, a high degree of compensation was sustained for many beacon-laser pulses. The long-term average Strehl ratio is 0.32, compared with 0.02 for the uncompensated images. Figure 17 shows the long-term average compensated and uncompensated images of Procyon.

SOURCES OF ERROR IN SYNTHETIC-BEACON ADAPTIVE OPTICS

SYNTHETIC-BEACON adaptive optics systems have several sources of error that degrade the quality of the atmospheric correction. The major sources of error are listed here with a brief explanation of their origin. Table A gives an estimate of the size of each error for the SWAT system. The error sources denoted with a star (*) are those specific to synthetic-beacon adaptive optics systems.

Fitting Error is due to the inability of the wavefront sensor to measure, and the deformable mirror to correct for, distortions with spatial wavelengths smaller than twice the subaperture spacing. This error also includes effects due to the aperture edges and central obscuration.

*Calibration error** is due to imperfect calibration of the adaptive optics components. Typically the largest contribution is from the deformable mirror.

*Time-delay error** results from atmospheric changes that take place between the measurement and correction cycles. This error depends on winds aloft. The time delay is analogous to the servo response time in a continuous-wave adaptive optics system.

Scintillation error is the degradation of the compensated image due to a nonuniform intensity distribution arising from scintillation.

Non-common-path error is due to optical aberrations measured by the wavefront sensor from a part of the system not common to the imaging optics.

*Focal anisoplanatic error** results from the adaptive optics beacon originating at a finite altitude. This includes not only unmeasured turbulence above the beacon altitude, but also the error due to the improperly measured distortion below the beacon altitude, resulting from the focused beacon geometry.

Wavefront-sensor noise error results from the finite number of synthetic-beacon photons detected by the wavefront sensor. Also included in this noise term is the readout noise from the cameras in the wavefront sensor.

Table A. Synthetic-Beacon Compensation Errors

Error Type	*Error Variance σ^2 (rad^2)*
Fitting error (subaperture spacing = 3.75 cm, r_0 = 10 cm)	0.02
Calibration error (deformable-mirror surface ~ $\lambda/25$)	0.25
Time-delay error (wind = 10 m/sec, τ = 500 μsec, r_0 = 10 cm)	0.05
Scintillation error (σ_x^2, r_0 = 10 cm)	0.03
Non-common-path error (~ $\lambda/20$)	0.01
Focal anisoplanatic error (beacon altitude = 6 km)	0.50
Wavefront-sensor noise error (~ $\lambda/15$)	0.18
Total error variance	1.04
Strehl ratio = $\exp(-\sigma^2)$	0.35

Angular Anisoplanatism

An angular offset between the synthetic beacon and the object being viewed introduces an additional source of error because the atmospheric turbulence being sampled by the beacon is not the same as the turbulence traversed by the light that arrives at the telescope from the object. As might be expected, high-altitude turbulence affects the angular anisoplanatic error more than turbulence at lower altitudes, because

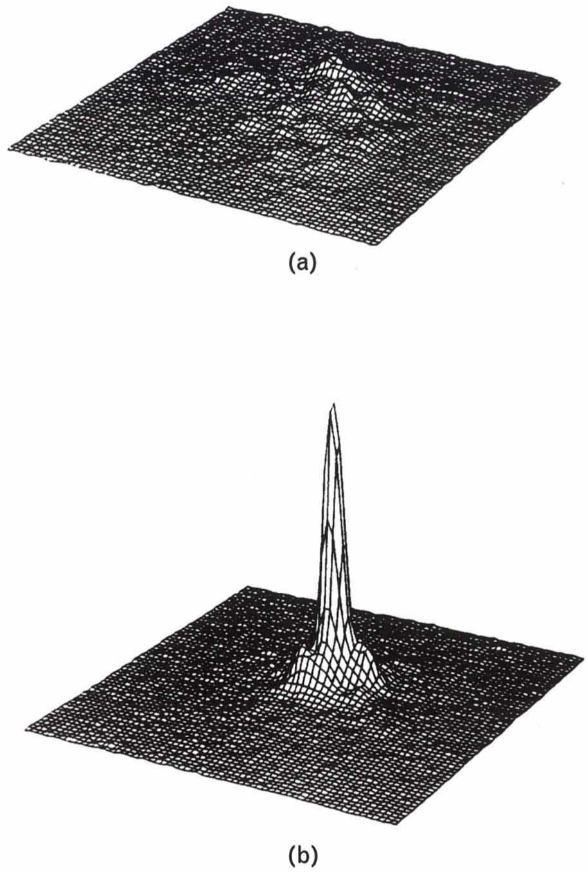

FIGURE 15. (a) Uncompensated and (b) compensated images of the star Procyon (α-Canis Major) on 6 February 1991. The compensated image has a Strehl ratio of 0.4. The measured atmospheric coherence length was 10 cm, and the measured isoplanatic angle was 20 μrad during acquisition of these data. The zenith angle of the star was 20°; the field of view is 19 μrad.

the displacement between the beacon and object ray paths is greatest at higher altitudes. Figure 18 shows the measured effects of angular anisoplanatism for atmospheric compensation with a synthetic beacon. The decrease in Strehl ratio with a larger beacon offset angle is apparent, although it is not a rapid decrease because of the finite beacon altitude used (in this case 6 km). For a 6-km beacon, even at offset angles as large as 50 μrad, the beacon focal spot has moved only to the edge of the column defined by the telescope aperture. Higher-altitude synthetic beacons are more sensitive to angular anisoplanatism, but of course they reduce the error from turbulence above the beacon altitude.

Temporal Phase Decorrelation

Because the atmosphere is dynamic, a wavefront correction based on a measurement made at one instant becomes less valid as time passes. At visible wavelengths, a phase measurement typically begins to lose its usefulness within a few milliseconds. Figure 19 shows the decay of image brightness with time, after a correction has been applied, based on a phase measurement using a single synthetic-beacon pulse. The data were taken by gating the star camera repetitively after the application of the phase correction to the deformable mirror. Exposures were separated by 2 msec, with each exposure lasting 1 msec. The Strehl ratio for each image was then calculated. Note that the Strehl ratio asymptotically approaches a value that is higher than when no adaptive optics compensation is applied. In the absence of any correction, the image of the star is degraded not only by the atmosphere but also by static aberrations in the optical train. The instantaneous correction made by the adaptive optics compensates for both these sources of aberration. As time passes, the correction corresponding to the static aberration remains valid; it determines the asymptote to which the Strehl ratio falls. With the asymptote as a baseline, Figure 19 shows the Strehl ratio falling to $1/e$ of its initial value in approximately 15 msec.

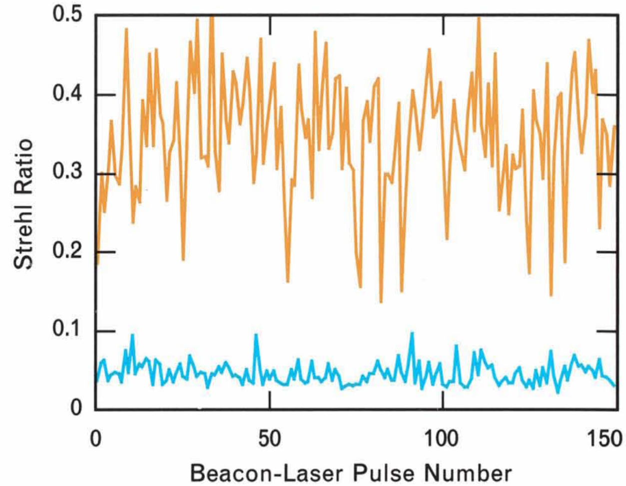

FIGURE 16. Uncompensated and compensated Strehl ratios for 150 consecutive synthetic-beacon experiments with the star Procyon, taken at a repetition rate of 2.5 Hz.

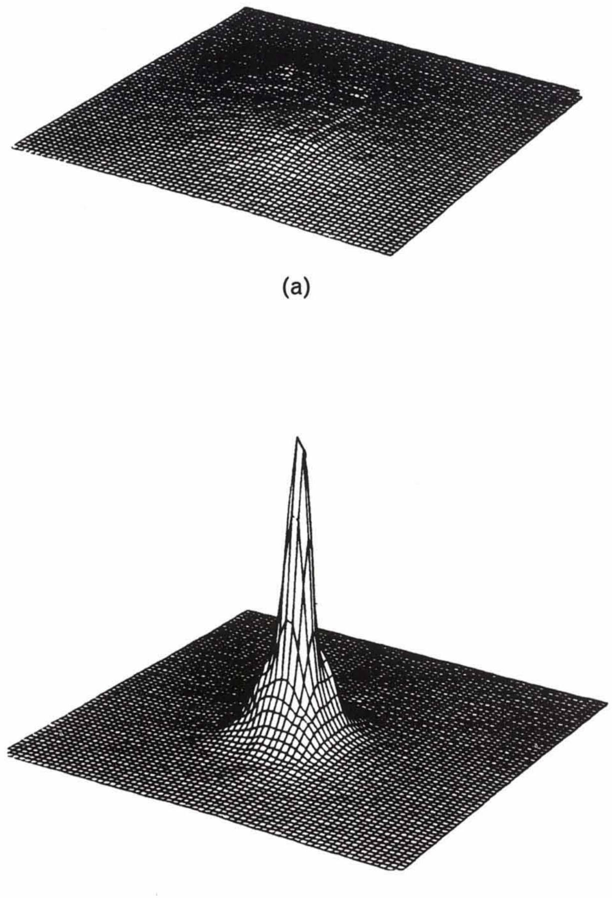

FIGURE 17. Long-term average images of the (a) uncompensated and (b) compensated images of the star Procyon. The field of view is 19 μrad. These images are the result of averaging the compensated and uncompensated images from the 150 Procyon compensation pulses (shown in Figure 15).

Multiple Synthetic-Beacon Experiments

For the 60-cm telescope used in the SWAT experiments, the turbulence measurement error associated with the ray geometry of a finite-altitude synthetic beacon is small. The error can be significant, however, when synthetic-beacon adaptive optics systems are used with apertures of much larger diameter. A way to reduce the error in a large-aperture system is to distribute an array of synthetic beacons in a regular pattern above the telescope, as shown in Figure 20. Then, for phase correction, the full-aperture gradient information from all of the beacons must be assembled, or *stitched* together, by the reconstructor hardware

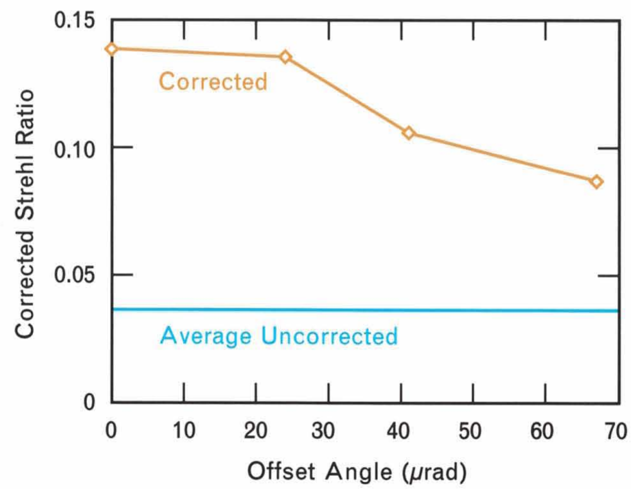

FIGURE 18. Decrease in the Strehl ratio with synthetic-beacon offset angle for the star Arcturus (α-Boötes). The Strehl ratio decreases with angle because the beacon starts to sample turbulence over paths different from those taken by the starlight.

into one overall phase that can be applied to the deformable mirror [20]. The reconstructor accomplishes this by first removing the average gradient (overall tilt) from the gradient data obtained from each beacon. Then the array of gradient data for each beacon is modified by discarding all gradients that lie outside the section of the aperture above which that

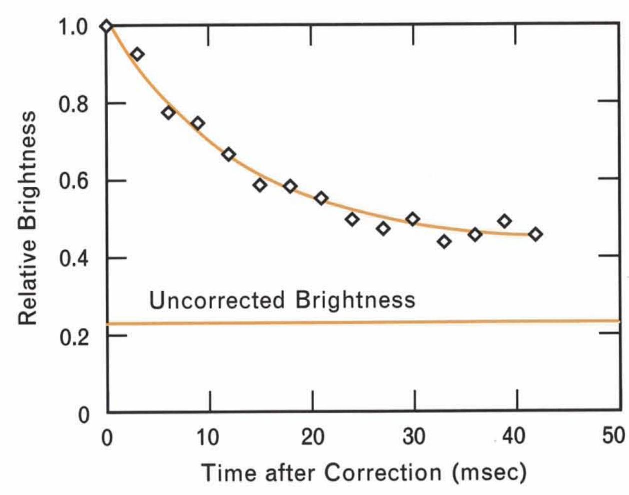

FIGURE 19. Decrease in the Strehl ratio with time after compensation due to the dynamic changes in atmospheric distortion. These changes result primarily from winds aloft moving the distortion through the path taken by the starlight to the telescope. The characteristic time for the atmospheric relaxation on this night was 15 msec.

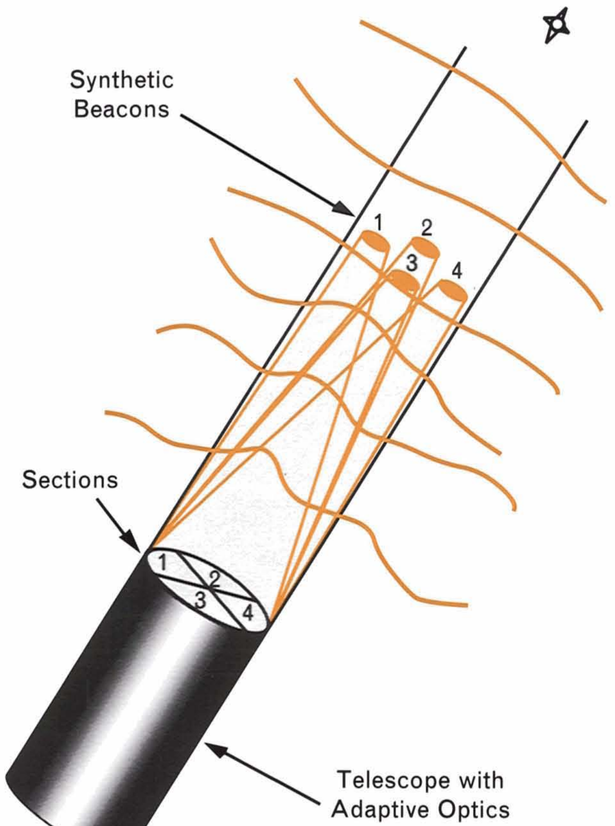

FIGURE 20. Measuring the atmospheric distortion with an array of synthetic beacons reduces the wavefront error due to focal anisoplanatism because of the more accurate sampling of turbulence close to the edges of the aperture.

beacon is placed. Next, the sections of gradient data are abutted to form a single set of gradients extending over the full aperture. These gradients are reconstructed into the phase correction and applied to the deformable mirror. The end result is a correction whose phase in a particular section of the aperture comes mainly from the gradient measurements of the beacon above that section. This method has the advantage of eliminating phase discontinuities at the boundaries between sections.

The SWAT system was designed to test the concept of using multiple synthetic beacons. Besides the additional reconstructor features, experiments with multiple beacons required components to multiplex the beacon laser beams and to place the beacons with precision relative to the line of sight of the telescope. For SWAT, we separated the beacon pulses in time so that returns from beacons in different locations could be distinguished and processed sequentially. (The interval between pulses had to be kept small, of course, so that the entire sequence occurred well before the atmosphere changed.)

Although the adaptive optics system was capable of using up to six synthetic beacons, we used only two in our experiments. Because of our small telescope aperture, the benefit of using more than one synthetic beacon to reduce focal anisoplanatism was small. Thus our two-beam tests were carried out not to show dramatic improvements in correction but to demonstrate a technical approach to multiple-beacon adaptive optics and the utility of the stitching concept.

Figure 21 shows a diagram of our approach with two lasers. The beams from the dye lasers converged at a well-defined angle to a point on the corner of the main optical bench, where a switching mirror, which could be rapidly switched in angle from one fixed position to another, was used to introduce a particular laser beam onto the system optical axis. Once on axis, two tilt mirrors imparted a selectable amount of tilt to the laser beam to place the beacon focal spot in the desired location above the telescope aperture. A second identical set of tilt mirrors, located in front of the wavefront sensor, was used to remove the tilt from the backscattered beacon radiation before the wavefront measurement. Figure 22 shows the overall system timing diagram for a two-beacon stitching experiment, and Figure 23 is a photograph of the switching mirrors and the tilt mirrors. The switching mirrors and both sets of tilt mirrors are commanded to the desired position approximately 200 μsec before the beacon laser is fired to ensure that they have settled.

Figure 24 compares the compensated image from a single-beacon experiment with an image taken by stitching together the wavefronts of two offset synthetic beacons. These images were taken a few minutes apart, under atmospheric conditions with r_0 equal to 5 cm and θ_0 equal to 13 μrad. The star used on this occasion was Pollux (β-Gemini), with a visual magnitude of 1.2; the zenith angle was 16°. The beacons were offset by ±25 μrad, which corresponds to ±15 cm at the beacon altitude of 6 km. The range depth for these experiments was 1.5 km. Figure 25 shows how the beacons were oriented relative to each other.

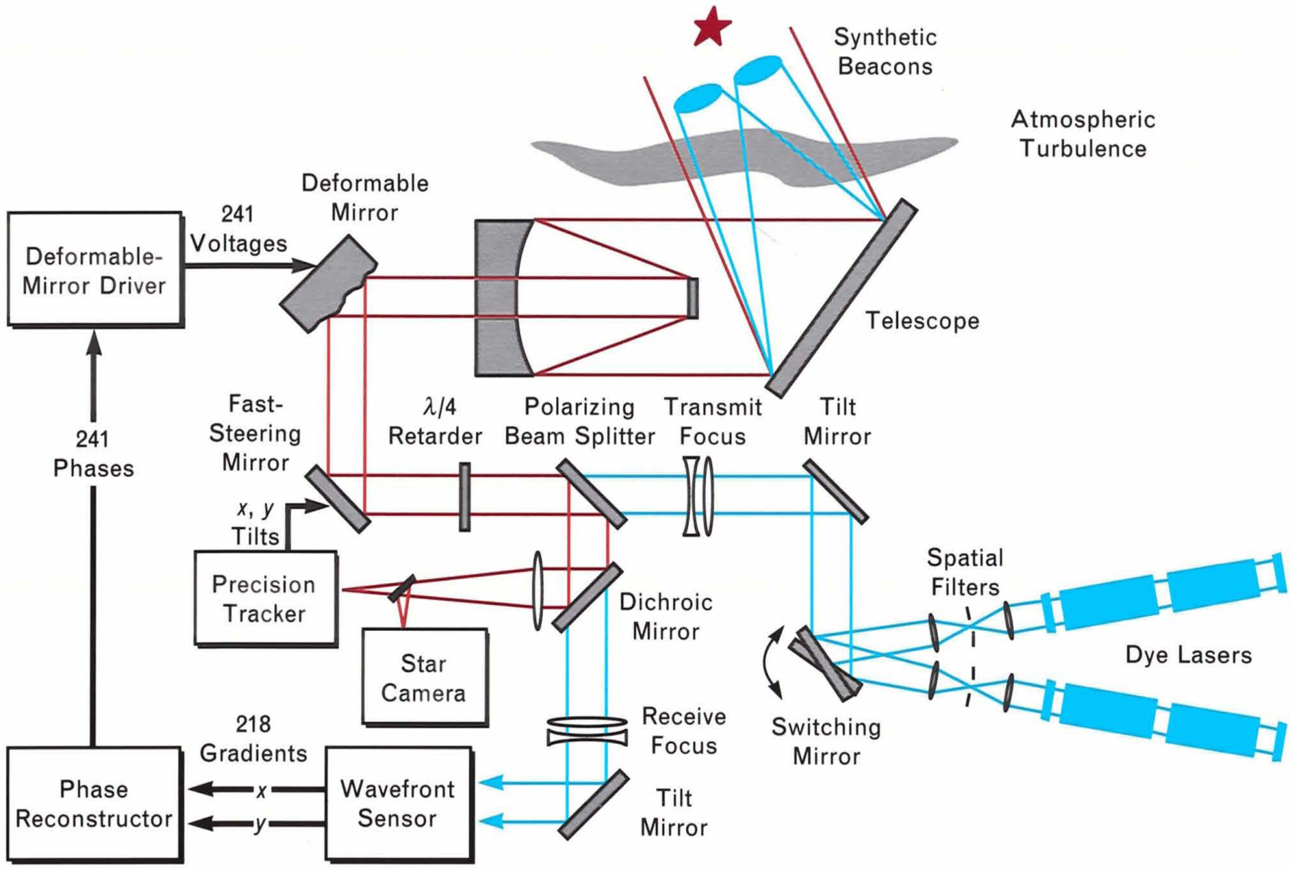

FIGURE 21. System schematic for compensation experiments using two synthetic beacons. These experiments require more components than the single-beacon experiments, primarily to multiplex the multiple beacon-laser pulses and to place the beacons at the appropriate positions above the telescope aperture.

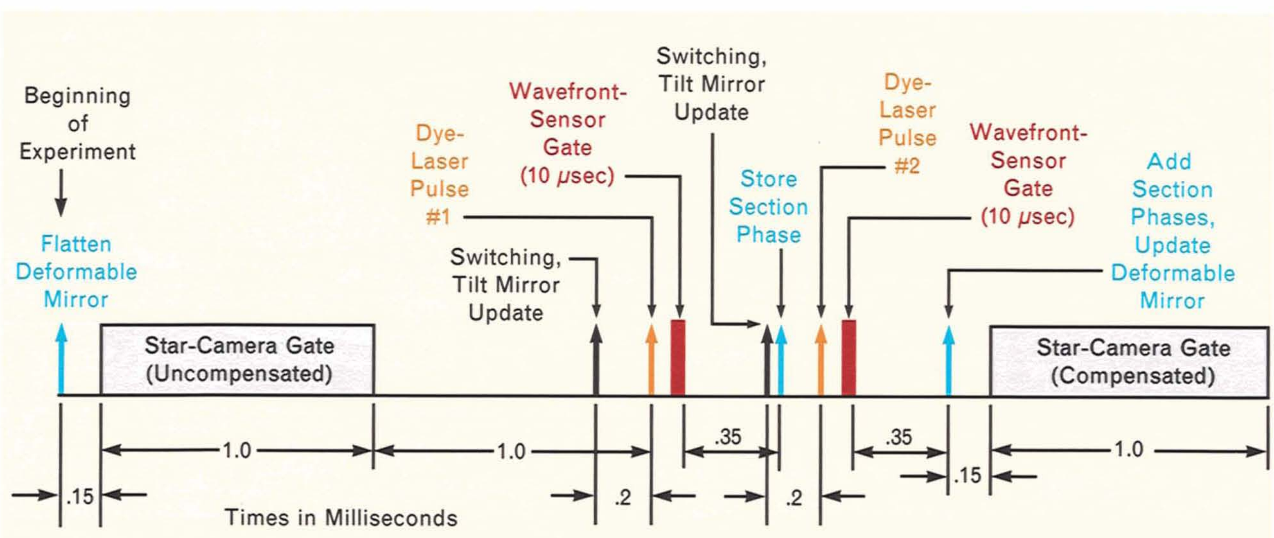

FIGURE 22. Event timeline for compensation experiments using two synthetic beacons. These experiments are more complex than their single-beacon counterparts because of the special phase reconstruction for stitching the individual beacons together and the need for switching and tilt mirrors. This timeline is repeated at a rate of 5 Hz.

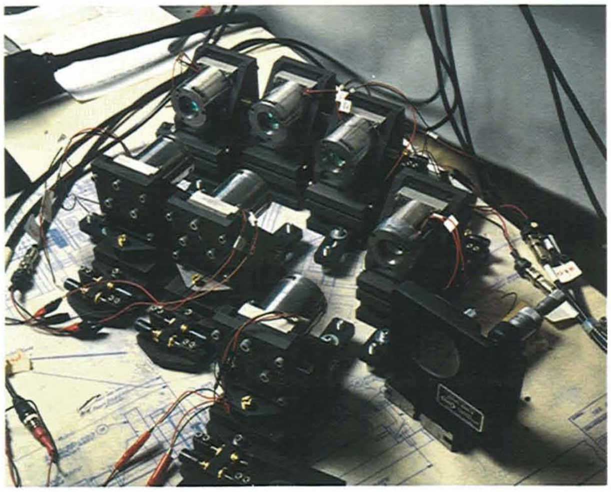

FIGURE 23. Photograph of switching and tilt mirrors. The mirrors are piezoelectrically actuated and are able to respond in 200 μsec. These mirrors bring the individual beacon lasers onto the optical axis of the adaptive optics system, then point the lasers slightly off axis to place each beam above the correct section of the telescope aperture.

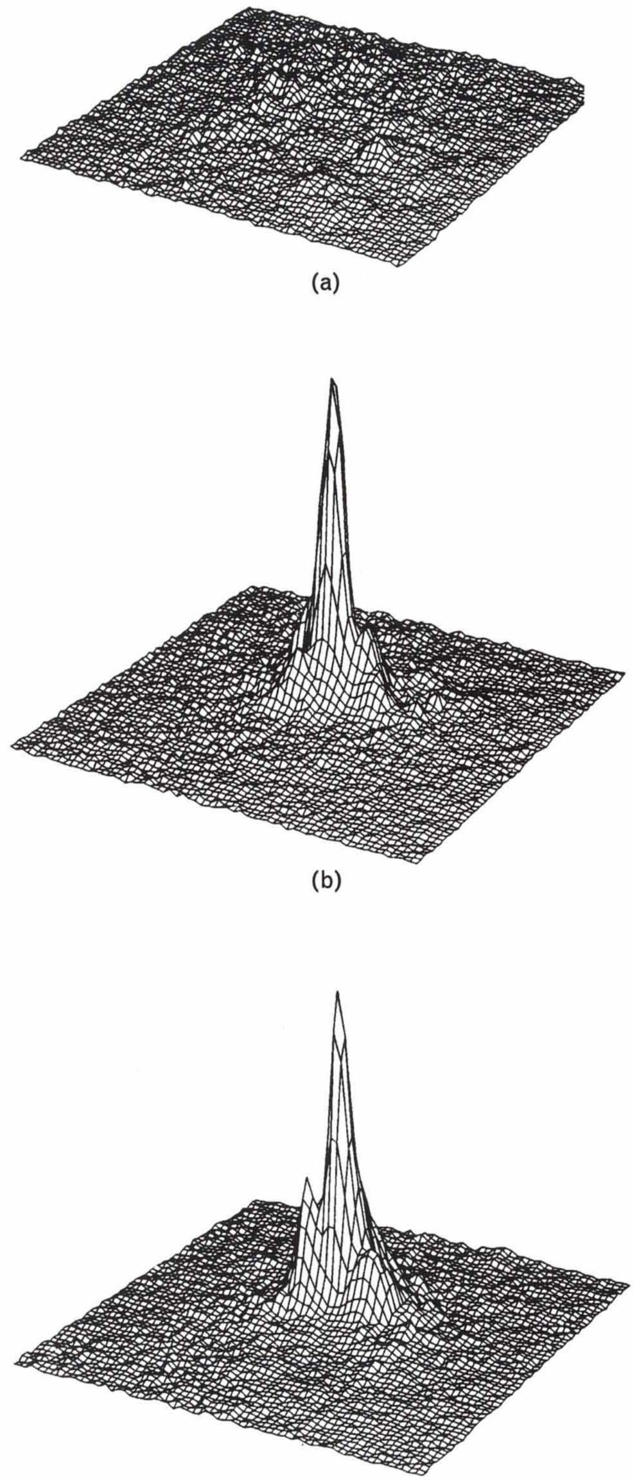

(a)

(b)

(c)

FIGURE 24. Comparison of compensated images of Pollux (β-Gemini), showing (a) an uncompensated image, (b) compensation using a single synthetic beacon, and (c) compensation using stitched data from two synthetic beacons. The field of view is 19 μrad.

As we expected, the differences in compensation between the two images are small, and are within the variability normally seen from one experimental run to the next. For these data, the compensated Strehl ratios were approximately 0.2 and the short-exposure uncompensated Strehl ratio was 0.02. This experiment demonstrates a feasible approach to creating multiple synthetic beacons and shows that good compensation can be obtained by combining the measurements made from beacons that are spatially separated. The techniques used are scalable to larger apertures and larger numbers of beacons.

Astrometry

Figure 26 shows compensated and uncompensated images of the multiple star system Yale 3482 (ε-Hydra). These data were acquired at a zenith angle of 40°, during atmospheric conditions with r_0 equal to 9.8 cm and θ_0 equal to 16 μrad (normalized to zenith). The star system is reported to have three main components [21], including two with visual magnitudes 3.8 and 4.7 that orbit each other with a separation of approximately 0.2 arc sec (1 μrad). These two components have an orbital period of 15 years. The third component has a visual magnitude of 6.8 and

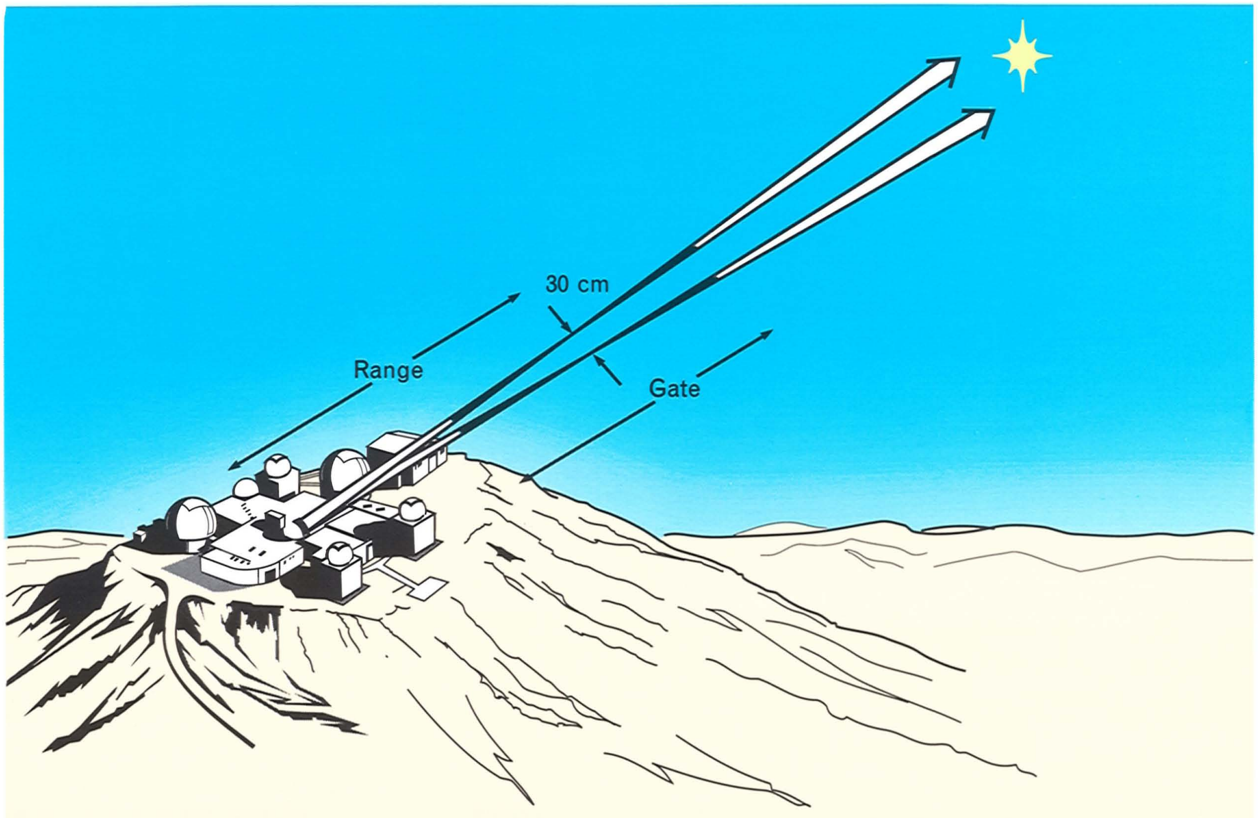

FIGURE 25. Multiple-beacon geometry for the Pollux data shown in Figure 24. The beacon range was 6 km, with a gate depth of 1.5 km, centered on the range. The beacons were offset from the optical axis by 25 μrad, which separated the beacon spots by approximately 30 cm at the beacon altitude.

orbits the close pair at a separation of 2.8 arc sec (13 μrad), which is outside the field of view of our star camera. The compensated image clearly shows the close components. Analysis of the image gives a measured separation of 0.21 arc sec, or 1.0 μrad, in agreement with the value reported in the literature. This angle is smaller than the usual seeing at all but the best astronomical sites under the best observing conditions. Thus most ground-based telescopes without adaptive optics are unable to resolve the individual components of this binary system because of the effects of atmospheric turbulence.

A computer-generated image of the same binary pair with the relative magnitudes, separation, and orientation reported in Reference 19 appears in Figure 27 for comparison. This image takes into account our 60-cm telescope's finite resolution, which is due to diffraction, as well as our imaging camera's measured point-spread-function, and represents what we would measure in the absence of atmospheric turbulence. Even though the measured star image has a Strehl ratio of only 0.2, and a fair amount of energy in broad shoulders, the width of the central peak is close to that of the diffraction-limited peak. This characteristic, which we see throughout our data, is one of the features of adaptive optics that make astrometry possible even with images of modest Strehl ratio.

As a final note, astrometry of stars such as ε-Hydra is usually done by using speckle-imaging techniques [22], which typically require hours of data acquisition and many more hours of offline processing of the data. In addition, the end result of the speckle-imaging processing is not an image of the object, but rather its autocorrelation. In contrast, the data presented here were selected from a set of images taken over a total time span of two minutes. Little processing other than simple background subtraction and frame averaging was required.

(a)

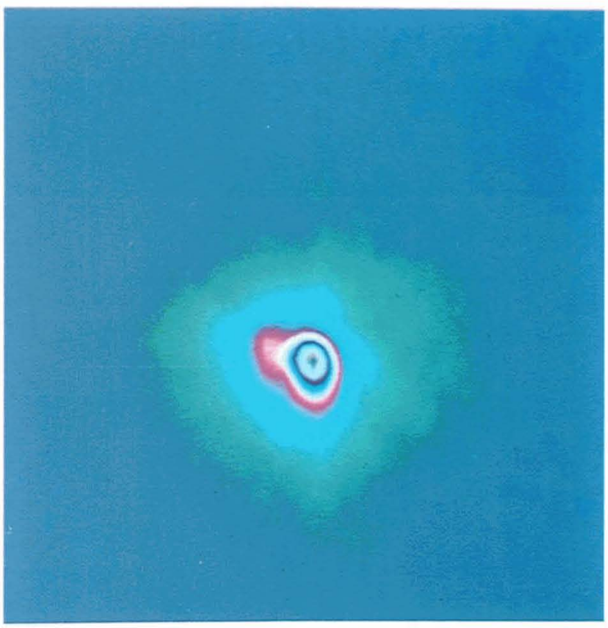

(b)

FIGURE 26. (a) Uncompensated and (b) compensated images of the star Yale 3482 (ε-Hydra), using a single synthetic beacon. This star system has two components in orbit around each other, with visual magnitudes of 3.8 and 4.7, separated by 1 μrad (0.2 arc sec). This separation angle is smaller than the atmospheric seeing at all but the best optical sites under the best observing conditions. The field of view is 19 μrad.

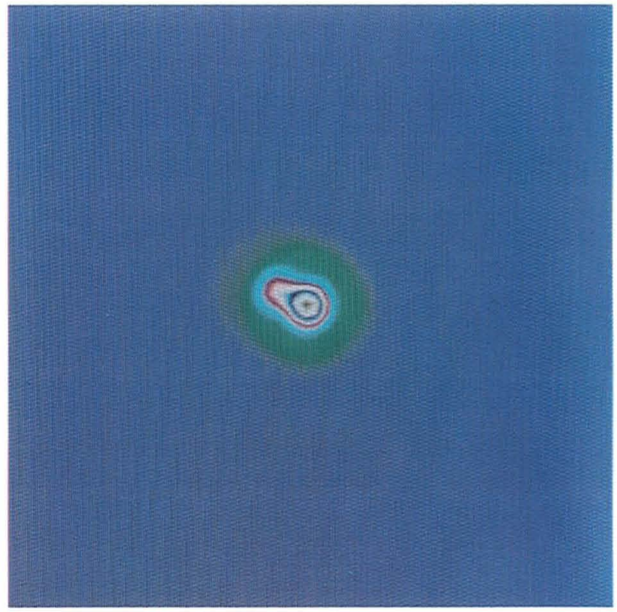

FIGURE 27. A computer-generated image of the binary star Yale 3482 (ε-Hydra), using the visual magnitudes, separation, and orientation found in Reference 19, and taking into account the effects of diffraction and optical transfer function for the SWAT imaging camera.

Summary

Compensation for the deleterious effects of atmospheric-turbulence-induced distortion can be achieved by using synthetic beacons in an adaptive optics system. Synthetic beacons allow us to compensate the images of dim astronomical objects, when a nearby bright guide star is not available. Compensation using both single and multiple synthetic beacons was demonstrated for the first time in SWAT experiments.

Acknowledgements

This work could not have been accomplished without a tremendous effort by everyone involved in the SWAT project. I would like to thank my colleagues: Robert Kramer for the system design; Bert Willard for the optical design; Ronald Parenti, Rich Sasiela, and John Shelton for their system performance predictions; Jan Herrmann and Lee Bradley for theoretical calculations; Linda Sue Sohn, Suzanne LePage, Harry Sagerian, and Martin Brennan for data analysis; Gregory Rowe for taking good care of the computer hardware and software; William McGonagle and Robert Reich for CCD focal planes; Brian Player and

Herb Barclay for providing outstanding hardware on short notice; Daniel Murphy, Jonathan Twichell, and Daniel Page, my fellow experimentalists; Frank Perry, Irving Wigdor, Patrick Everett, Pete Smith and Pete Rossini for system design and engineering; Robert Carlson, Emory Ariel, and Herbert Feinstein for mechanical engineering; Thomas Price for shaking down the prototype dye lasers and calibrating the deformable mirror; Charles Primmerman, Jack Lifsitz, Ronald Humphreys, and Darryl Greenwood for guidance and focus. Finally, to the individuals who lived and worked at the Maui Field Site—you deserve special thanks, for your lives were profoundly affected by the frenetic pace and long hours: Jerry Black, Lewis Chaulk, Lewis Farrar, Robert Hatch, Fred Huettig, Robert Ludwig, Joseph Mahan, James Swedberg, and Paul Szarko.

REFERENCES

1. D.P. Greenwood and C.A. Primmerman, "Adaptive Optics Research at Lincoln Laboratory," in this issue.
2. R. Foy and A. Labeyrie, "Feasibility of Adaptive Telescope with Laser Probe," *Astron. Astrophys.* **152**, L29 (1985).
3. R.A. Humphreys, L.C. Bradley, and J. Herrmann, "Sodium-Layer Synthetic Beacons for Adaptive Optics," in this issue.
4. C.A. Primmerman, D.V. Murphy, D.A. Page, B.G. Zollars, and H.T. Barclay, "Compensation of Atmospheric Optical Distortion Using a Synthetic Beacon," *Nature* **353**, 141 (1991).
5. D.V. Murphy, "Atmospheric-Turbulence Compensation Experiments Using Cooperative Beacons," in this issue.
6. R.R. Parenti, "Adaptive Optics for Astronomy," in this issue.
7. R.A. Humphreys, C.A. Primmerman, L.C. Bradley, and J. Herrmann, "Atmospheric-Turbulence Measurements Using a Synthetic Beacon in the Mesospheric Sodium Layer," *Opt. Lett.* **16**, 1367 (1991).
8. M.R. Bowman, A.J. Gibson, and M.C.W. Sandford, "Atmospheric Sodium Measured by a Tuned Laser Radar," *Nature* **221**, 456 (1969).
9. J.E. Blamont, M.L. Chanin, and G. Megie, "Vertical Distribution and Temperature Profile of the Nighttime Atmospheric Sodium Layer Obtained by Laser Backscatter," *Ann. Geophys.* **28**, 833 (1972).
10. T.H. Jeys, A.A. Brailove, and A. Mooradian, "Sum Frequency Generation of Sodium Resonance Radiation," *Appl. Opt.* **28**, 2588 (1989).
11. P.N. Everett, H.R. Aldag, J.J. Ehrlich, G.S. Janes, D.E. Klimek, F.M. Landers, and D.P. Pacheco, "Efficient 7-J Flashlamp-Pumped Dye Laser at 500-nm Wavelength," *Appl. Opt.* **25**, 2142 (1986).
12. M.A. Easley and J.F. Washeba, "Continuous Facesheet Low Voltage Deformable Mirrors," *Opt. Eng.* **29**, 1191 (1990).
13. H.T. Barclay, P.H. Malyak, W.H. McGonagle, R.K. Reich, G.S. Rowe, and J.C. Twichell, "The SWAT Wavefront Sensor," in this issue.
14. R.J. Sasiela and J.G. Mooney, "An Optical Phase Reconstructor Based on Using a Multiplier-Accumulator Approach," *Proc. SPIE* **551**, 170 (1985).
15. J. Herrmann, "Least-Squares Wave Front Errors of Minimum Norm," *J. Opt. Soc. Am.* **70**, 28 (1980).
16. A.E. Siegman, "Modes in Unstable Optical Resonators and Lens Waveguides," *IEEE J. Quantum Electron.* **3**, 156 (1967).
17. P.N. Everett and B.G. Zollars, "Engineering of a Multi-Beam 300-Watt Flashlamp-Pumped Dye-Laser System," *Proc. Intl. Conf. on Lasers, 1987* (STS Press, McLean, VA, 1988), p. 291.
18. D.L. Fried, "Optical Resolution through a Randomly Inhomogeneous Medium for Very Long and Very Short Exposures," *J. Opt. Soc. Am.* **56**, 1372 (1966).
19. D.L. Walters, "Saturation and the Zenith Angle Dependence of Atmospheric Isoplanatic Angle Measurements," *Proc. SPIE* **551**, 38 (1985).
20. D.V. Murphy, C.A. Primmerman, B.G. Zollars, and H.T. Barclay, "Experimental Demonstration of Atmospheric Compensation using Multiple Synthetic Beacons," *Opt. Lett.* **16**, 1797 (1991).
21. A. Hirshfeld and R. Sinnot, eds., *Sky Catalog 2000.0, Vol. 2: Double Stars, Variable Stars, and Non-Stellar Objects* (Cambridge University Press and Sky Publishing Corp., 1985).
22. W.I. Beavers, D.E. Dudgeon, J.W. Beletic, and M.T. Lane, "Speckle Imaging through the Atmosphere," *Lincoln Laboratory J.* **2**, 207 (1989).

BYRON G. ZOLLARS
is a staff member in the High-Energy-Laser Beam Control and Propagation group. His area of research is in adaptive optics laser-beam propagation through the atmosphere. Byron received his B.S. degree in physics from Texas A&M University, and his M.S. and Ph.D. degrees in physics from Rice University. He has been at Lincoln Laboratory since 1986.